Climate Dynamics
https://doi.org/10.1007/s00382-021-05822-9

# Improved boreal summer intraseasonal oscillation simulations over the Indian Ocean by modifying moist parameterizations in climate models

Young-Min Yang[1] · Jeong-A Cho[3] · Ja-Yeon Moon[3] · Ki-Young Kim[3] · Bin Wang[1,2]

Received: 14 December 2020 / Accepted: 18 May 2021


**Abstract**
Northward propagation of the boreal summer intraseasonal oscillation (BSISO) system over the Indian Ocean significantly affects Asia summer monsoon and extreme weather events including typhoons but many climate models poorly simulate the norward movement of BSISO. Here, we suggest that the modified parameterizations can improve BSISO northward propagation and three-dimensional dynamic and thermodynamic structures by enhancing the vorticity anomalies under the mean vertical wind shear and meridional gradient of mean moisture in the climate models. We hypothesize that poor BSISO simulation in a climate model may result from too frequent deep convections without abundant moisture in the boundary layer (BL). To represent them, the modified parameterizations include (a) a BL depth-dependent convective trigger, (b) a bottom-heavy diffusivity in the shallow convection scheme, (c) Relative humidity-dependent convective entrainment rate, and (d) reduced conversion rate of convective cloud water to rainwater. The modified parameterizations increase vertical shear over the northern Indian Ocean by strengthened easterly anomalies in the upper troposphere, inducing positive barotropic vorticity anomalies. The enhanced positive vorticities generate boundary layer moisture convergence and positive convective instability in the north of the BSISO convection center, inducing next convection and thereby improving northward propagation of the BSISO. The modified parameterizations also improve the meridional gradient of mean-moisture advection in the lower troposphere with increasing upward transport of moisture in the boundary layer. The increased air-sea interaction by modified parameterization tends to intensify the signal of the northward movement of the BSISO. It is shown that the modified parameterizations work properly in different types of convective parameterizations. The possibility that our hypothesis may be applied to other climate models for improvement of the BSISO northward propagation is discussed.

**Keywords** Boreal summer intraseasonal oscillation · Northward propagation · Convective parameterizations · NESM3.0 · Air-sea interaction · GloSea5

## 1 Introduction

Boreal summer intraseasonal oscillation (BSISO) exhibits robust northward propagation in the Indian Ocean (e.g., Wang and Rui 1990; Zhu and Wang 1993; Hsu and Weng 2001). In the Indian Ocean, the BSISO northward propagation begins near the equator, extends to the subtropical western Pacific, affecting the East Asian summer monsoon (e.g., Wang and Xie 1997; Lee et al. 2013, 2017; Li et al. 2015; Hsu et al. 2017; Yang et al. 2010), typhoon activities (Maloney and Hartmann 2001; Goswami et al. 2003; Kikuchi et al. 2009; Moon et al. 2018), and extreme weather events (Moon et al. 2013; Hsu et al. 2016, 2017).

Many processes and mechanisms have been suggested to explain the northward propagation of BSISO in the western

✉ Ja-Yeon Moon
mjy1011@gmail.com

[1] Department of Atmospheric Science, Key Laboratory of Meteorological Disaster of Ministry of Education, Joint International Research Laboratory of Climate and Environment Change, Collaborative Innovation Center on Forecast and Evaluation of Meteorological Disasters and Earth System Modeling Center, Nanjing University of Information Science and Technology, Nanjing 210044, China

[2] Department of Atmospheric Sciences and International Pacific Research Center, University of Hawaii, Honolulu, HI, USA

[3] Research Institute, 4D Solution Co. Ltd., Seoul, South Korea

Published online: 29 May 2021

North Pacific (WNP) and the Indian Ocean, including air-sea interaction, vorticity anomalies induced by vertical wind shear, and meridional moisture advection. Hsu and Weng (2001) found that positive feedback between anomalous circulation and convection leads to enhanced evaporation over the oceans (e.g. South China Sea) and moisture transport northeastward. Kemball-Cook and Weare (2001) suggested that sea surface temperature (SST) is likely to be warmer at the north of the BSISO precipitation center due to enhanced net radiation at the surface with reduced wind speed, which may be more favorable for convection moving northward. The increased SST anomalies induced by air-sea interaction enhance convective instability to the north of convection, thus moving the convection northward (Fu et al. 2003; Fu and Wang 2004; Zheng et al. 2004). Katsumata et al. (2011) proposed that pre-moistening due to warmer SST anomalies at the north of the BSISO center might be critical for the northward propagation of ISO precipitation. The dynamic theories encompassing wave dynamics and vorticity-wind shear interaction have been proposed to explain the northward propagation of BSISO (Wang and Xie 1997; Jiang et al. 2004; Drbohlav and Wang 2005; Yang et al. 2019a, 2020c). Jiang et al. (2004) suggested that northward propagation of ISO convection may be generated by generating a boundary layer (BL) moisture convergence to the north of the BSISO precipitation center. The BL moisture convergence may be caused by barotropic vorticity anomalies by vertical shear. DeMott et al. (2013) found that the boundary layer moisture advection and barotropic vorticity effect are major processes for the northward propagation of BSISO precipitation. Yang et al. (2019a) demonstrated that the interaction among wave dynamics, vorticity anomalies, and vertical wind shear is the dominant process for BSISO northward propagation in the Indian Ocean. On the other hand, Stephens et al. (2002) and Simmons et al. (2007) used satellite data and found that cloud water in the lower troposphere occurs north of the ISO convection center, which may contribute to the northward propagation of BSISO.

In the climate models, previous studies showed that BSISO northward propagation can be improved by the modification of moist physical processes (Kang et al. 2010; Liu et al. 2015, 2018; Abhik et al. 2013; Ganai et al. 2019; Chattopadhyay et al. 2009; Halder et al. 2012). Neena et al. (2017) attempted to identify the key using the multi-model and found that the meridional structure of lower tropospheric zonal wind, temperature, and diabatic heating anomalies associated with BSISO may play a critical role in improving northward propagation simulations. A few studies focused on the role of convective momentum transport, which may induce northward propagation of BSISO (Kang et al. 2010; Liu et al. 2015). For example, Kang et al. (2010) showed that a secondary meridional circulation by convective momentum transports may generate BL convergence with strong easterly shear. The effect of shallow convection has been emphasized by Liu et al. (2018) and Abhik et al. (2013). They suggested that the shallow convection may enhance BSISO propagation northward by generating shallow convection at the north of the BSISO convective center. Liu et al. (2015) show that the meridional gradient of humidity fields by shallow convection contributes to generating the frictional convergence at the north of the BSISO. Recent studies (Ganai et al. 2019; Chattopadhyay et al. 2009; Halder et al. 2012) revealed that the northward propagation of BSISO may be improved by representing realistic grid-scale cloud processes and enhanced large-scale heating.

Our study utilizes a recently developed earth system model, the Nanjing University of Information Science and Technology (NUIST) Earth System Model version 3 (NESM3) (Cao et al. 2018; Yang et al. 2020a). The NESM3.0 reproduces reasonable climatology and realistic MJO and BSISO (Yang and Wang 2019; Yang et al. 2019a, b, 2020b). In the model simulations, the northward propagation of BSISO is well reproduced over both the WNP and Indian Ocean. We modified moist physical processes in the atmosphere of NESM3.0 and examine the role of air-sea interaction, meridional moisture advection, and vorticity anomalies by zonal vertical shear on BSISO northward propagation. The explanation for the modified parameterizations and model experiments is described in Sects. 2 and 3. We examine dominant mechanisms for improved BSISO northward propagation in different parameterizations using various diagnostics in Sect. 4. Section 5 summarizes our findings.

## 2 The model and diagnostic methods

### 2.1 Model and experiments

The NESM3.0 includes atmosphere, ocean, land, and sea ice components. The details of the model are described in Cao et al. (2018) and Yang et al. (2020a). The horizontal resolution of the atmosphere model is T63 (about 200 km) and its vertical resolution is 47 levels. The ocean model has a resolution of 1° latitude and longitude grid with the meridional resolution being refined to 1/3° over the equatorial region, and it has 46 vertical layers with the first 15 layers at the top 100 m. The sea ice model resolution is about 1° latitude by longitude with four sea ice layers and one snow layer on the top of the ice surface. The convective parameterization is based on Tiedtke (1989) (TDK, hereafter), and the default setting is from the European Centre Hamburg Atmospheric model version6.3 (ECHAM6.3) (Peters et al. 2017 and; Möbis and Stevens 2012). The stratiform cloud scheme implements a cloud microphysical scheme and a diagnostic cloud cover scheme. This convective scheme includes

three different convection types- shallow, deep, and midlevel convection but in the convective scheme, only one type of convective scheme is allowed in one vertical column at a given time. The initiation of deep convection is dependent on the magnitude of large-scale moisture convergence. The buoyance of updrafts is affected by organized entrainment and detrainment and the entrainment rate is calculated by buoyancy and vertical velocity of the updraft. The closure of the deep convection scheme is calculated by convective available potential energy (CAPE) (Nordeng 1994).

### 2.2 The data and diagnostic methods

The Global Precipitation Climatology Project (GPCP) daily data (Adler et al. 2003) are used for precipitation, and the European Center for Medium-Range Weather Forecast Reanalysis (ERA) Interim daily data (Dee et al. 2011) are utilized for circulation during 1997–2014. We used a 20–70-day band-pass filter to obtain the ISO signal during the boreal summer season (May 1st to October 31st). We analyzed the relationship between circulation, SST and moisture, and ISO northward propagation based on dynamics-based diagnostics. The vertical shear is defined by the difference in zonal winds between 200 and 850 hPa (U200–U850) averaged over 80°E and 100°E. Our strategy is to use coupled model experiments to examine the impacts of the model's parametrization changes on the model's simulations because the modified parameterizations may affect the coupled model climatology and variability. The second principle is to use comprehensive metrics including both climatology and ISO perturbation. Because some change of parameterizations targeted for the improvement of ISO northward propagation may degrade the model's performance (e.g. climatology) in other aspects.

## 3 Improvement of the model physical parameterizations

### 3.1 The original model's deficiencies and possible causes

The ISO convection in the earlier version of the model does not propagate northward. From the zonal vertical shear theory (Jiang et al. 2004) and global climate models' diagnostics (Neena et al. 2017), the meridional structure of lower tropospheric wind, moisture, temperature and diabatic heating anomalies concerning ISO deep convection may play a critical key for better northward propagation. Also, the implementation of the shallow convection may improve the northward propagation of the BSISO by enhancing upward transport of the moisture at the north of the ISO center (Liu et al. 2018; Abhik et al. 2013), which may be favorable for the occurrence of next deep convection at the north of the BSISO center. Yang et al. (2019a) suggested that lower tropospheric heating, which can induce next convection at the north of the BSISO center may be critical for realistic ISO simulation. The enhancing shallow convection may improve the northward propagation of ISO precipitation by enhancing the interaction between lower tropospheric heating and boundary layer moisture convergence (BLMC) and gradual transition from shallow to deep convection. Given the problems with the early version, we improved the model's capacity in simulating both ISO propagation and realistic climatology.

### 3.2 Major modifications and tunings made to the parameterization schemes

One of the major problems in the CTL simulation is the warm SST bias in the tropics, which influences both mean precipitation and BSISO, and also large-scale circulations. It may be due to incorrect cloudiness or cloud-radiation interaction. We examined the role of cloudiness on warm SST bias by increasing cloudiness. The warm SST biases were significantly reduced by reducing the amount of solar radiation downward but BSISO northward propagation and the precipitation climatology were little improved, suggesting that we need to modify moist physics processes, particularly convective parameterization because most precipitation is made by a convective scheme in the eastern Indian ocean from the model simulations. We hypothesize that the poor BSISO simulation may result from too frequent deep convection without abundant lower tropospheric moisture and associated convective instability. The earlier NESM3.0 shows less sensitivity to lower tropospheric moisture (e.g. Yang et al. 2020b), which is far from the observation. In the observation, the precipitation increase with increasing low-level moisture, indicating that deep convection or heavy rainfall may occur when a deep moist boundary layer developed or convective instability is accumulated properly (Kim et al. 2011, 2014). To represent those hypotheses, our strategy is allowing deep convection for abundant moisture in the lower troposphere. To do this, we used (1) convective trigger based on boundary layer moisture, (2) enhance shallow convection to transport moisture near boundary layer to free atmosphere, (3) entrainment rate based on relative humidity, which allows deep convection when relative humidity is relatively large, (4) reducing the conversion rate from convective cloud water to rain in the convective scheme, which tends to suppress convective rainfall.

### 3.2.1 The modified TDK scheme

The convective parameterizations were modified in the NESM3.0. We implemented a convective trigger to the convective scheme (hereafter 'TRIG'; Yang et al. 2018; Yang and Wang 2019). This trigger is based on the Tokioka constraint (Tokioka et al. 1988) and further modified. The original Tokioka constraint was designed for a "multiple-cloud (updraft)" mass flux scheme (e.g. the Arakawa-Schubert scheme). The original Tokioka constraint does not generate a deep convective cloud for relatively shallow PBL depths. Because the TDK scheme used a single updraft, the deep cloud tends to be suppressed too much and enhance large-scale condensation to remove convective instability with colder SST by increases the cloudiness in coupled models. To reduce the negative effect of the Tokioka constraint, different criteria to determine the initiation of each cloud type are utilized. We use relaxed criteria for deep and middle convection compared to that for shallow convection. The modification may generate more frequent deep convection when compared to the same criteria for all cloud types.

$$\varepsilon_{min} = \frac{a_i}{h}, \quad \begin{matrix} \text{convection turns off, if } \varepsilon \le \varepsilon_{min} \\ \text{convection turns on, if } \varepsilon > \varepsilon_{min} \end{matrix}, \tag{1}$$

where i refers to cloud type (deep, midlevel, and shallow convection), h is the BL depth, $\varepsilon_{min}$ is minimum entrainment rate, and $a_i$ is a constant. The TRIG does not generate convection for relatively shallow BL depth. We adopt different constants for deep convection ($a_i = 0.005$), shallow ($a_i = 0.015$), midlevel ($a_i = 0.010$) respectively. Those values may help to reduce colder SST simulation by the original Tokioka constraint. In the western Pacific, colder SST may occur compared to other regions because suppressed convection may induce large-scale condensation due to relatively high humidity. However, in the Indian ocean, this effect is relatively small, inducing weak cooling in the surface (e.g. Fig. 1e).

Second, a shallow convection scheme (SHLC) with a bottom-heavy diffusivity (Yang and Wang 2019) was included. This scheme is modified from Tiedtke et al. (1988). This scheme calculated the following diffusive terms for large scale (grid mean) dry static energy S and specific humidity q (Tiedtke et al. 1988):

$$\frac{\partial \bar{s}}{\partial t} = \frac{1}{\bar{\rho}} \frac{\partial}{\partial z} \left\{ \bar{\rho} K \frac{\partial}{\partial z} \left( \bar{s} - L\bar{l} \right) \right\}, \tag{2}$$

$$\frac{\partial \bar{q}}{\partial t} = \frac{1}{\bar{\rho}} \frac{\partial}{\partial z} \left\{ \bar{\rho} K \frac{\partial}{\partial z} \left( \bar{q} + \bar{l} \right) \right\}, \tag{3}$$

where l represents cloud liquid water content, ρ the air density, L the latent heat, t the time, and z the height. The coefficient K is the eddy diffusivity showing a prescribed function of height. In earlier NESM3.0, it is shown that the vertical mixing between the boundary layer and lower troposphere is relatively weak, inducing less moisture and diabatic heating. Our shallow convection scheme includes a specific vertical profile of vertical mixing below 600 hPa; the vertical mixing near 925 hPa is relatively heavy and then gradually reduces to zero at 600 hPa. The new shallow convective scheme effectively enhanced shallow convection in the lower troposphere. It is known that the lower tropospheric heating to the north of BSISO deep convection may play a role in improving BSISO simulation (Liu et al. 2018; Abhik et al. 2013).

Third, the conversion rate from convective cloud water to rain in the convective scheme is modified (hereafter 'CPRCON'). This parameter changes the amount of convective precipitation and detrainment of remaining cloud water in the updraft to the ambient air, affecting the formation of the stratiform cloud. We modified the conversion rate of cloud water to rain (Gp) in the convective scheme. This process is assumed to be in proportion to liquid water in the cloud (l) and empirical function (K) that varies with height (Tiedtke 1989).

$$Gp = K(z)l, \tag{4}$$

where l is the liquid water content in the cloud and K(z) is constant at height, $2 \times 10^{-3}$. This parameter is reduced by 30% compared to the original value. Note that this change is in a general range of observed variability (Yanai et al. 1973). This parameter affects the convective precipitation, downdraft, and re-evaporation below the cloud-base, inducing a change of surface circulation and temperature. By reducing this parameter, the convection is suppressed and grid-scale precipitation can be enhanced.

Fourth, the entrainment rates in convective clouds were increased (hereafter 'ENTR'). An increasing entrainment rate may generate a decrease of deep convection since mixing between updraft and relatively dry and cold environmental air. In the convective scheme, cloud top is determined by entrainment rate, which is estimated by convective velocity and buoyancy of convective clouds (Möbis and Stevens 2012). In this study, we consider the impact of the relative humidity of the environmental air. The formula for entrainment rate as following: an entrainment rate (ε) is parameterized based on buoyancy (B_u) and grid-mean humidity (RH) based on Kim and Kang (2012)

$$\varepsilon = a_0 \times c_\varepsilon \times B_u, \quad c_\varepsilon = \frac{1}{RH}, \tag{5}$$

where, $a_0$ refers buoyancy on entrainment rate, and $c_\varepsilon$ are conversion factors of grid-mean humidity. When RH is low (< 10%), $c_\varepsilon$ is fixed at 10. For high RH (> 99%), $c_\varepsilon$ is $1 \cdot e - 1$. The range of entrainment rate is from $1 \cdot e^{-6}$ to $1 \cdot e^{-2}$ $m^{-1}$. The

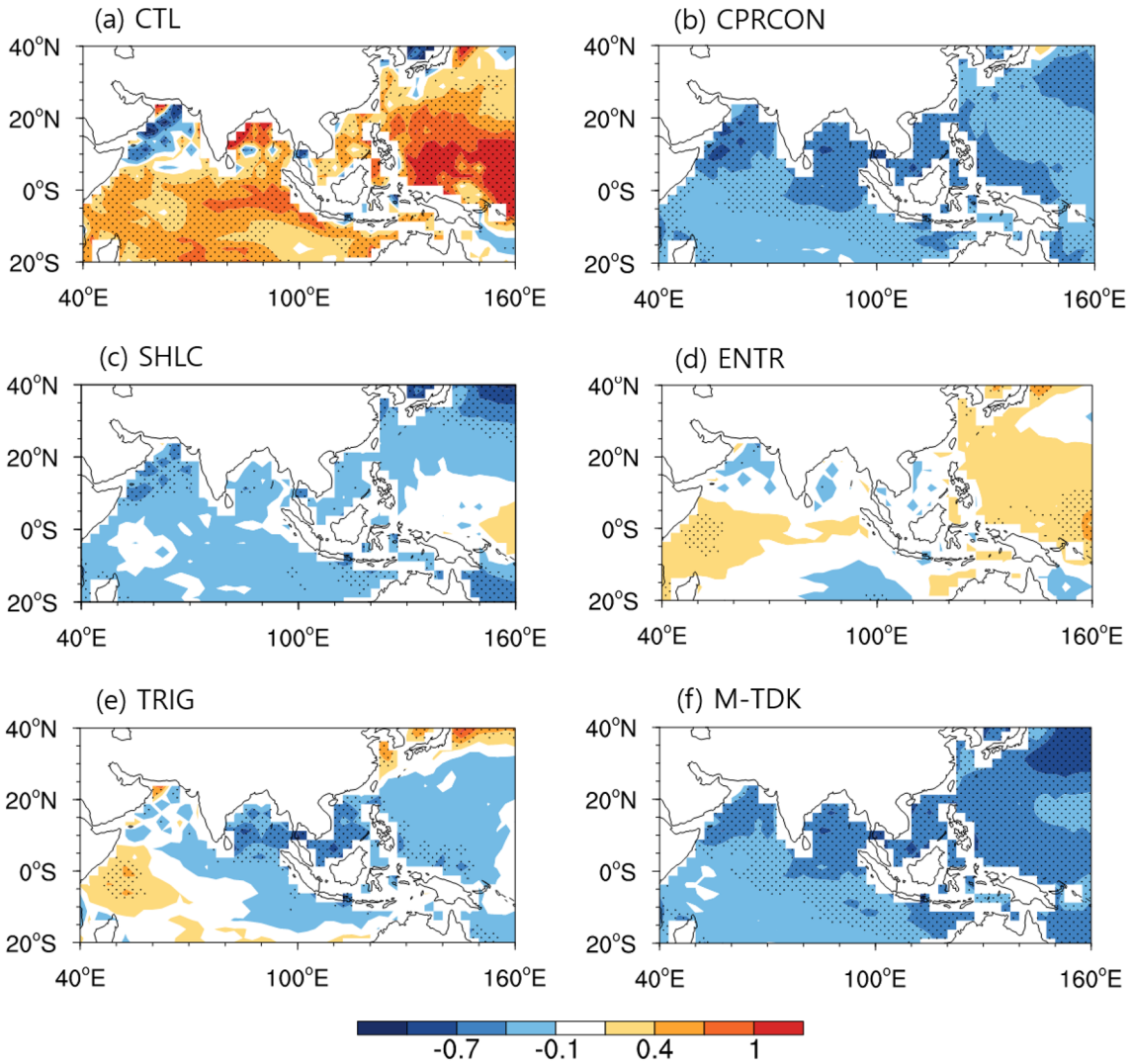


**Fig. 1** Bias of boreal summer (June–August) mean-state sea surface temperature (ºC) from the models with the modified parameterizations. Stippling indicates the region with statistically significant change at a 95% confidence level based on the t-test

second iteration occurs when the cloud depth (that is, the difference of lift condensation level and the level of neutral buoyancy) is larger than 200 hPa. For the second iteration, deep convection uses a pre-defined entrainment profile. We increase the entrainment rate for deep convection by 50% of the original value.

### 3.2.2 The modified RAS scheme

The relaxed Arakawa Schubert (RAS, Lee et al. 2001) scheme is included in the NESM3.0 model to examine that the modified schemes used in the TDK scheme work in other convective schemes. The RAS scheme has different characteristics compared to the TDK scheme. First, the RAS scheme generates multiple updrafts (it is called "cloud ensemble"), whereas the TDK scheme uses a single updraft. Second, the RAS assumes that all type of clouds in a grid is to develop but the TDK generates only one type of clouds among shallow, midlevel and deep clouds. Third, the RAS calculates the entrainment rate based on assumption that the buoyancy of updraft is zero at the cloud top, which is prescribed in the scheme, while the entrainment rate in the TDK is estimated with the updraft buoyancy. The TRIG, SHLC, CPRCON are also implemented into the RAS scheme. Note that ENTR is not included in the RAS scheme since the entrainment rate in the RAS scheme is determined by a prescribed cloud top.

We conducted six experiments by using the TDK scheme to test the impacts of modified parameterizations: (1) the original TDK without modification (CTL), (2) the TDK with the convective trigger (TRIG), (3) the TDK with the modified shallow convection (SHLC), (4) the TDK with

the modified ratio of convective cloud water to rainwater (CPRCON), (5) the TDK with the modified entrainment rate (ENTR), and (6) the TDK with all modifications (M-TDK). Two additional experiments are performed using the RAS scheme. One is the RAS scheme without the modifications (RAS), and the RAS scheme with combined TRIG, SHLC, and CPRCON (hereafter 'M-RAS'). Noted that the models have not been retuned for each change of the convective parameterizations. Because the model is fully coupled, we integrated the model through four stages. First, to obtain stable upper and deep ocean initial condition, only ocean model of the NESM3.0 integrated for 4000 years with atmospheric forcings. Second, to obtain a stable atmosphere–ocean equilibrium state, the NESM3.0 integrated for 500 years with an initial condition of the 4000 years ocean simulation and preindustrial forcings based on CMIP6 protocol. Third, to obtain initial conditions at 1990 years, the model has integrated for 140 years (1850–1990) with an initial condition of 500 years preindustrial simulation and historical CMIP6 forcings. Fourth, the model integrated for 50 years with an initial condition of 1990 years from 140 years historical simulation and the fixed CMIP6 external forcings averaged over 1990 to 1999. Note that we used 1990's fixed forcings to remove the impact of global warming. The last 20 years data of the 50 years simulations are used for analysis. The NESMs with the modified TDK and RAS schemes use the same parameter settings to facilitate comparison.

## 4 Effects of the modified parameterizations on mean fields and BSISO

### 4.1 Changes in the boreal summer mean climate

Figure 1 shows SST bias from the models with the modified parameterizations. The CTL shows a moderate warm bias over Indian and strong warming in the western Pacific and East Asia region. The meridional SST gradient decrease from the equatorial eastern Indian ocean to 10°N, while it tends to increase around 10°N to the Bay of Bengal. Compared to the CTL, the SST biases in the models with the modified parameterizations produces slightly weak cold biases in most Indian and western Pacific regions except ENTR. The CPRCON and TRIG produce moderate colder SST near the eastern Indian Ocean and western Pacific. The SHLC shows weak cold biases in the Indian ocean and subtropical western Pacific. The ENTR show relatively weak warming in the western Pacific and western Indian ocean. Since the CTL produces strong warm biases in those regions, those colder SST biases simulated by the modified parameterizations can contribute to reduced SST biases. The M-TDK shows a similar cold SST pattern with those of the CPRCON and the TRIG slightly stronger magnitude.

The change of SST pattern may induce a change of precipitation (Fig. 2). The CTL shows strong wet biases in the eastern Indian Ocean and western Pacific but moderate wet biases in the western Indian ocean. There are weak dry biases in the south of the Indian ocean and northwestern Pacific. The CPRCON, SHLC, and the M-TDK reduce both wet anomalies in the Indian Ocean and western Pacific and dry anomalies in the south of the Indian ocean. The ENTR and TRIG slightly reduce wet anomalies in the eastern Indian Ocean and western Pacific. In all models, the changes of horizontal patterns in precipitation are consistent with those of the SST change.

The change of precipitation by the modified parameterizations affects the circulation. Figure 3 shows zonal wind biases of the CTL and the modified models. The CTL simulates westerly bias in the eastern Indian Ocean and western Pacific, while easterly biases in the East China Sea and south of the Arabian sea. The CPRCON, SHLC, ENTR, and TRIG shows weakened westerly biases in the Indian Ocean and western Pacific and reduce easterly biases in the East China Sea and south of the Arabian sea, which is favorable with a decrease of the zonal wind bias shown in the CTL. The zonal wind is strongly reduced in the CPRCON and TRIG but relatively weak in the SHLC and ENTR. It may be attributed to the change of zonal gradient of mean SST. The strong cooling (warming) in the western Pacific (western Indian ocean) leads to anomalous sinking (rising) motions, inducing anomalous easterlies in the Indian ocean. The M-TDK produces weak westerly biases in the eastern Indian ocean.

To examine the structures of BSISO propagation over the Indian ocean in the models, We showed the phase 2 to phase 4 in the composite life cycles of outgoing longwave radiation (OLR) and horizontal wind vectors at 850 hPa associated with the BSISO in Fig. 4. These phases are calculated by the first two major modes of BSISO during May–October. We first calculated daily anomalies of OLR and zonal wind at 850 hPa (U850) (10°S–10°N, 40°–160°E) and applied multivariate empirical orthogonal function analysis (Lee et al. 2013). Eight phases are defined based on the first and second EOF mode which represents the canonical northward propagating mode. The observations show that, in phase 2, broad ISO positive convection anomalies in the Indian ocean and its peak is located at equatorial eastern Indian Ocean (EIO). The strong convective anomalies propagate northward from the EIO to the Bay of Bengal and also moves eastward to the Maritime continent and western Pacific at phase 3. In phase 4, the convective anomalies in the EIO move northward but their magnitude is significantly weakened and weak negative convective anomalies occur in the equatorial EIO. The CTL may fail to simulate the northward propagation of the ISO because of its weak initial intensity and deficiency of processes associated with the northward

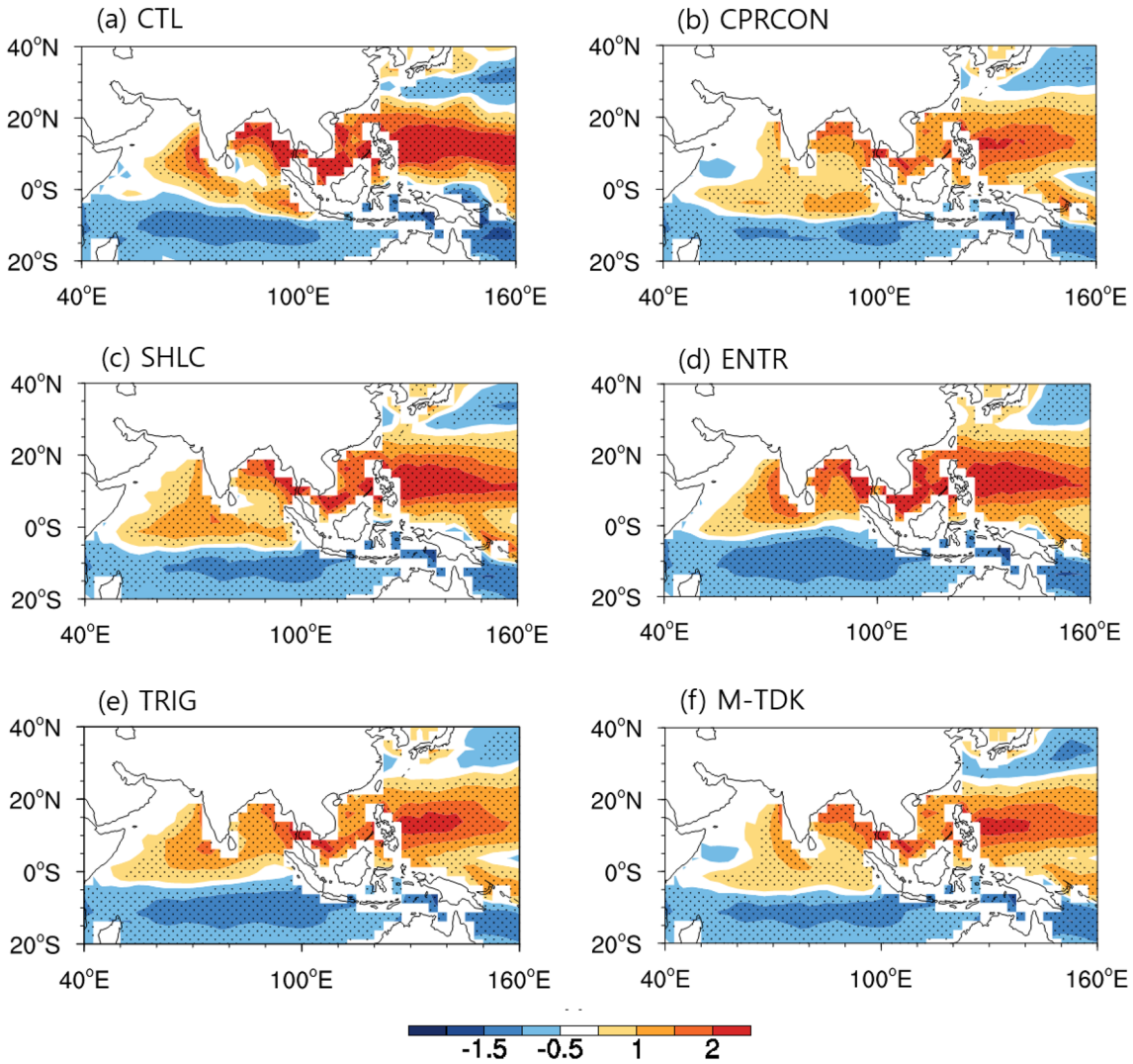


**Fig. 2** The bias of boreal summer (June–August) mean-state precipitation (mm day$^{-1}$) from the models with the modified parameterizations. Stippling indicates the region with statistically significant change at a 95% confidence level based on the t test

propagation of the ISO. The weak convective anomalies occur at the Bay of Bengal in phase 2. The convective anomalies in the eastern Indian ocean become strong and slightly move southward in phase 3. The convective anomalies eventually become weak and move to the south of the EIO in phase 4. Note that the CTL also does not reproduce eastward propagation from EIO to the western Pacific during phases 2 and 4. The CPRCON shows relatively strong convective anomalies in equatorial EIO at phase 2 and it tends to move northward at phase 3 with strong magnitude and then it becomes weak at phase 4. Note that the CPRCON does not reproduce eastward propagation of ISO from EIO to the east of the Philippine sea. The SHLC produces moderate ISO convection at phase 2and it propagate northward at phase 3. The convective anomalies are weakened in the Bay of Bengal and move eastward to the Philippine sea at phase 4, suggesting that the SHLC may improve both northward and eastward propagation. The ENTR simulates better northward propagation in the EIO with a reasonable horizontal pattern during phases 3 and 4. Note that the ENTR also improves eastward propagation to the western Pacific but the signal in the Maritime continent is relatively weak. The TRIG produces strong northward propagation of convective anomalies but its magnitudes are much stronger than the observation. The M-TDK reproduces the observed northward (or eastward) propagation in the EIO and western Pacific with relatively strong anomalies. The corresponding wind anomalies are also similar to the observation. Note that convection of the models tends to react more strongly to given SST

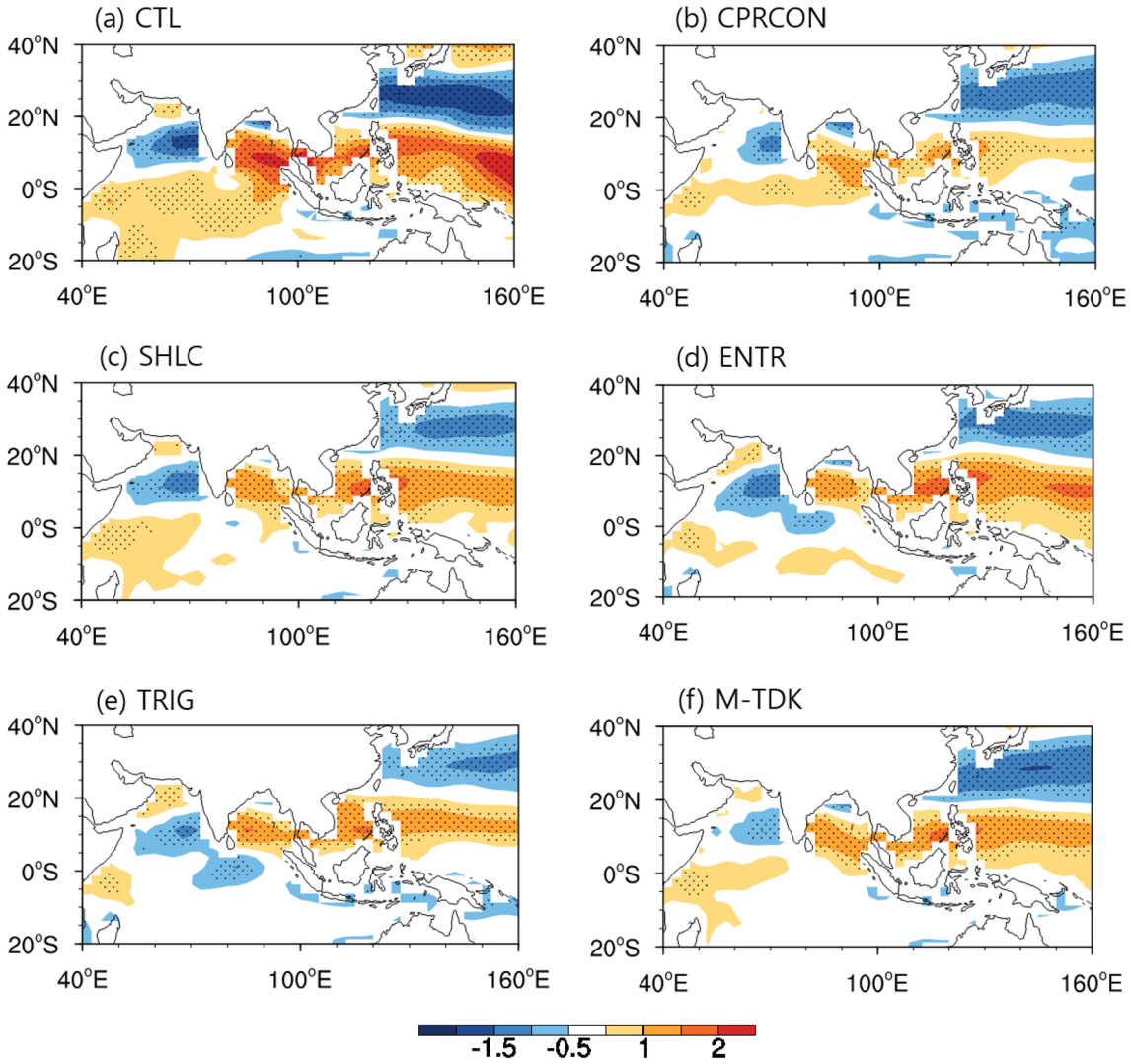


**Fig. 3** The bias of boreal summer (June–August) zonal wind at 850 hPa (m $s^{-1}$) from the models with the modified parameterizations. Stippling indicates the region with statistically significant change at a 95% confidence level based on the t test

compared to the observation, inducing more strong ISO convection.

### 4.2 Changes in BSISO properties

Analysis of climate model experiments indicates that mean-field changes due to the modified parameterizations systematically improve the BSISO northward propagation in the EIO, providing a good opportunity for better parameterizations to improve the propagation.

Figure 5 shows the latitude-time structure of the lead-lag correlation of BSISO precipitation in the EIO. We use the ISO convection center at the equatorial EIO (80°–100°E, 5°S–5°N) as a reference because strong BSISO northward propagation occurs there. In observations, the convection of the BSISO moves northward with a phase speed of 1.0 m $s^{-1}$ from equatorial EIO to the Bay of Bengal. The CTL fails to produce northward propagation of ISO convection. It seems to propagate southward with a slightly faster speed. The CPRCON and ENTR show improved northward propagation of ISO precipitation between 0°N–20°N with a relatively significant pattern correlation coefficient (> 0.7) when compared to the observation (Fig. 5a). The SHLC and TRIG produce dominant northward propagating ISO from equatorial EIO to the Bay of the Bengal with a moderate pattern correlation coefficient. The M-TDK successfully reproduces ISO northward propagation with a similar magnitude but the phase speed of BSISO is about 1.2 m $s^{-1}$, which is faster than the observation. These results suggest that the modified parameterizations tend to improve the northward propagation of the ISO simulation significantly.

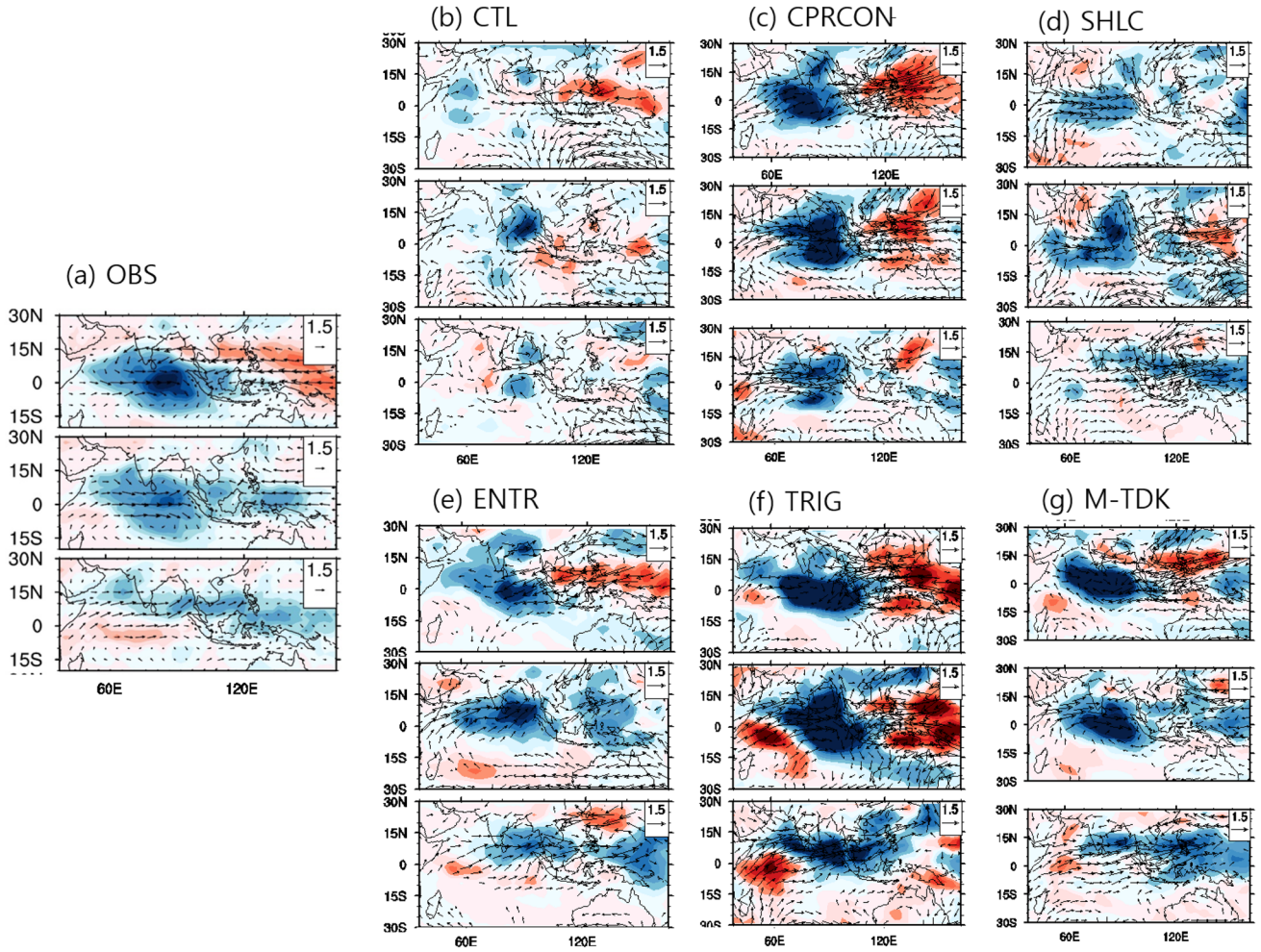


**Fig. 4** The life cycle composite of OLR (shading) and 850-hPa wind (vector) anomaly. Wind vectors are shown in the region with statistically significant change at a 95% confidence level based on a t test. We showed the phase 2 to phase 4 (top to bottom) obtained from **a** observation, **b**–**g** the model with the modified parameterizations. These phases are calculated by the first two major modes of BSISO during May–October. We first calculated daily anomalies of OLR and zonal wind at 850 hPa (U850) (10°S–10°N, 40°–160°E) and applied multivariate empirical orthogonal function analysis (Lee et al. 2013). Eight phases are defined based on the first and second EOF mode which represents the canonical northward propagating mode

### 4.3 Causes of the changes of ISO simulations with the modified parameterizations

We examine how mean state changes by the modified parameterizations affect the ISO northward propagation over the EIO. The modified parameterization tends to suppress deep convection, while enhances shallow or congestus clouds, which changes the JJA mean vertical zonal wind shear by modifying temperature and wind fields in the lower and higher troposphere (Fig. 6a). In the observation, dominant easterly vertical shear averaged over the EIO (80°E–100°E) was seen from the EIO and Bay of Bengal (10°S–30°N). The vertical shear has a peak around 10°N and then reduced with increasing latitude. The CTL simulates weak shear from south of EIO to the Bay of Bengal and its peak is much smaller than the observation (50%), which is far from the observations. When compared to the CTL, the models with the modified parameterizations simulate a realistic meridional structure of zonal shear with a slightly strong magnitude around 10°N by thermodynamic and dynamic effects of the modified parameterizations. The M-TDK and CPRCON show stronger zonal vertical shear than observation.

The enhanced zonal vertical shear can generate coupled baroclinic and barotropic modes, inducing a change of barotropic vorticity anomaly (Wang and Xie 1997; Xie and Wang 1996). Figure 6d show vorticity anomalies (925 hPa) regressed on the 20–70 day filtered precipitation averaged over the eastern Indian ocean (5°S–5°N, 80°–100°E). Observation shows significant positive vorticity anomalies from 5°N to 15°N, where zonal vertical shear is about 25 m $s^{-1}$. Its peak is located around 10°N, which is consistent with the range of northward propagation of the ISO precipitation

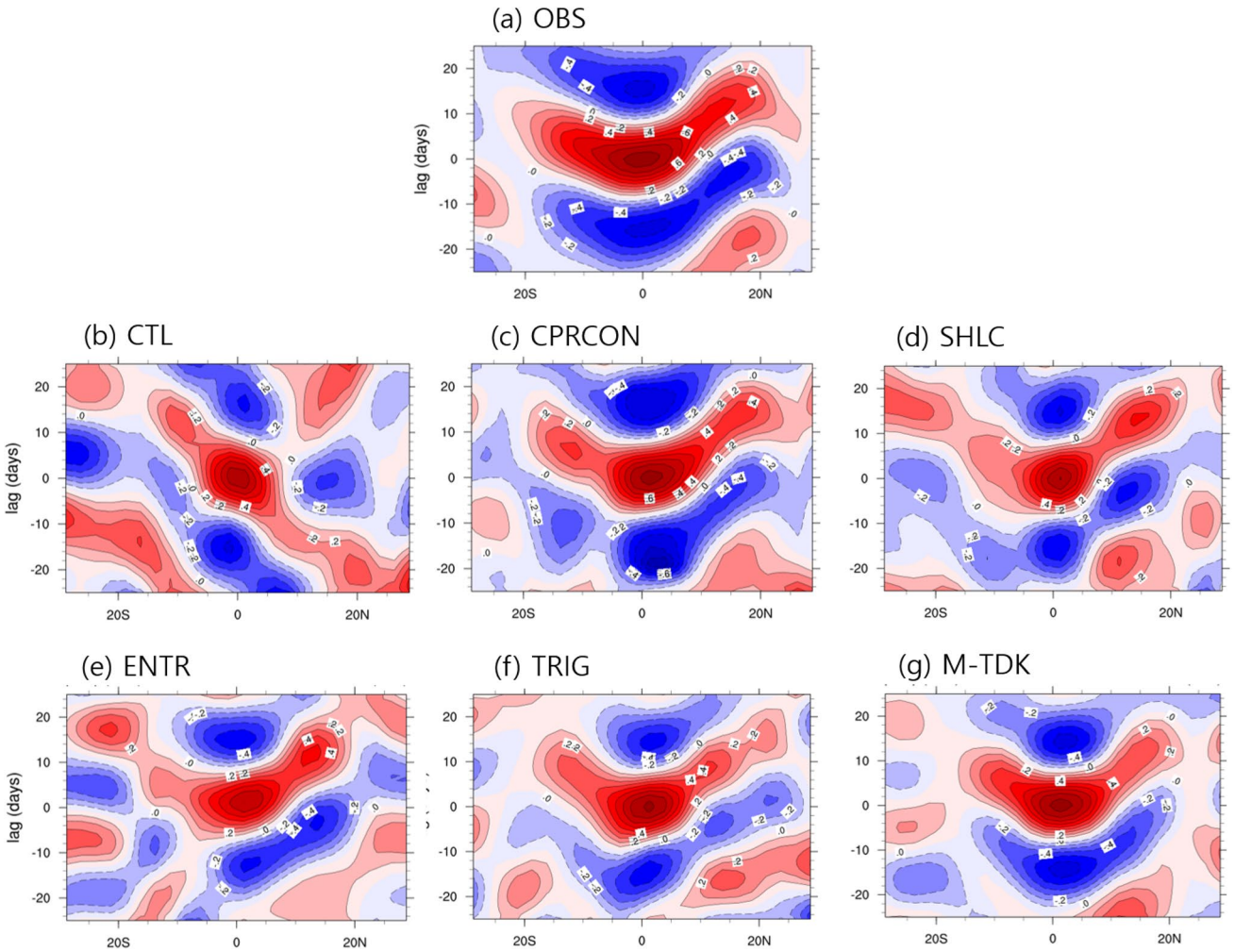


**Fig. 5** Propagation of ISO precipitation as depicted by the lead-lag correlation of 20–70 day filtered precipitation averaged over 80°–100°E from **a** observation and **b–g** the model simulations with the modified parameterizations during boreal summer (May–October). The ISO precipitation averaged over 80°–100°E and 5°S–5°N was used as a reference for calculating the correlation

center (e.g., Jiang et al. 2004). In the CTL, the positive vorticity anomalies are weak between 5°N and 15°N, which may be consistent with corresponding weak vertical shear. The models with the modified parameterizations simulate strong positive vorticity anomalies from the EIO to 15°N, which are similar to the observed. These results suggest that the changes in vorticity anomalies may be attributed to the magnitude of vertical wind shear. The magnitude of vorticity in the M-TDK is almost the same as that of the observation. The magnitudes of cyclonic vorticity in the model are enhanced and the corresponding northward propagation signal of ISO convection is also improved, implying that the positive vorticity anomalies may be the primary factor for the generation of the next convection north of BSISO center in the EIO.

The change of vorticity anomalies may generate BLMC. Figure 6e represents BLMC anomalies (925 hPa) regressed on the 20–70 day filtered precipitation averaged over the eastern Indian Ocean (5°S–5°N, 80°–100°E). The observation shows the positive anomalies of the BLMC over 5°S to 15°N. The peak is located near the equator and extends northward, indicating that the next convection may be generated to the north of the ISO center. In the CTL, the positive BLMC anomalies occur only 5°S to 10°N and the magnitude is also weaker than the observation. The modified parameterizations tend to increase the BLMC anomalies. The CPRCON simulates stronger BLMC than that of the CTL, showing broader positive anomalies than the CTL between 10°S and 15°N. The ENTR and SHLC also enhance the meridional structure of the BLMC anomalies with a stronger magnitude than the observation. The TRIG significantly intensifies the BLMC anomalies than the ENTR and SHLC. The M-TDK produces realistic BLMC anomalies with a relatively strong magnitude. These results, compared

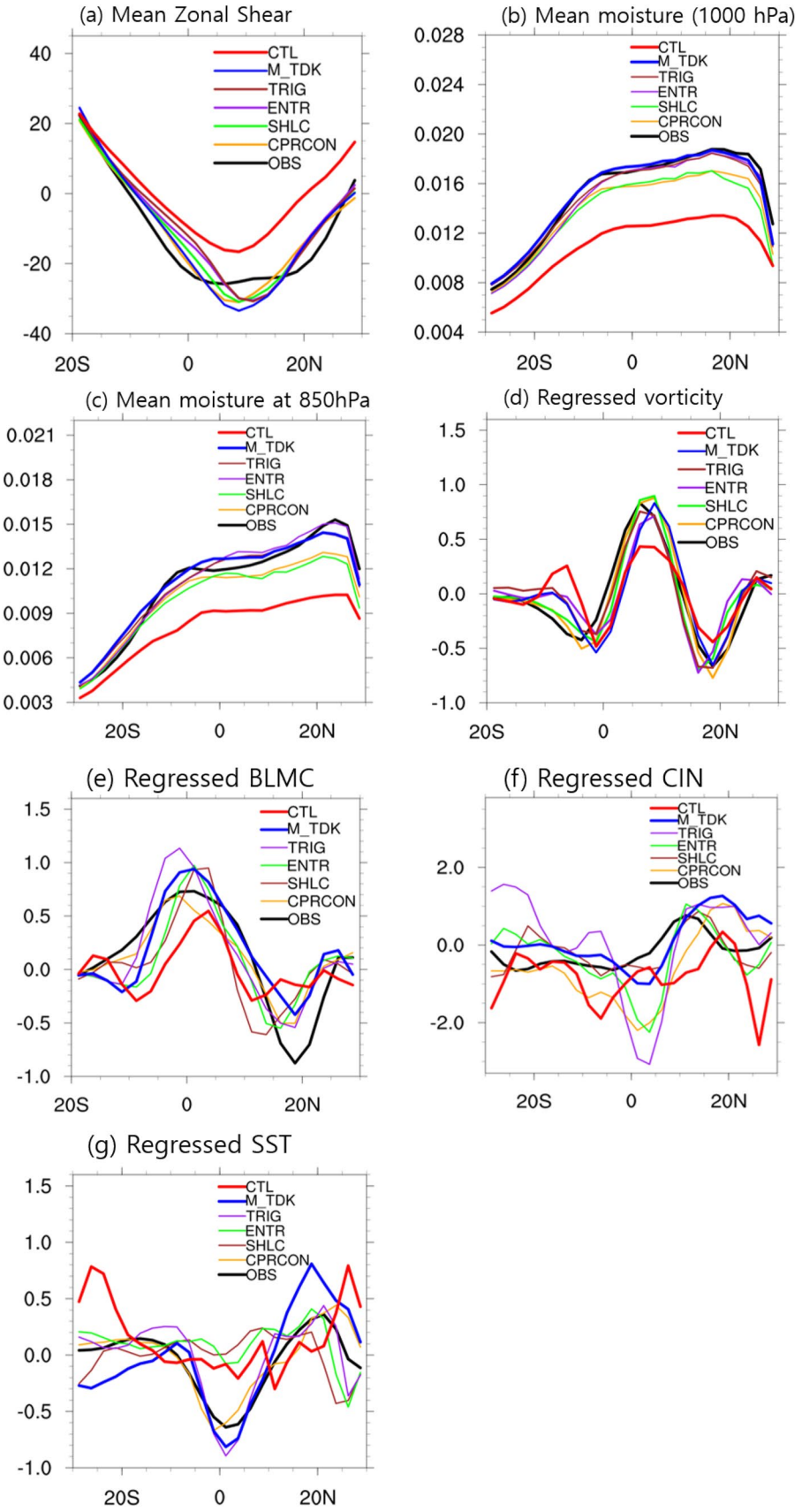


**Fig. 6** Meridional structure of June–August **a** mean-state zonal shear (U200–U850), **b** mean specific humidity at **b** 1000 hPa, and **c** 850 hPa averaged over 80°–100°E from observation (black line) and the models (colored line). Meridional variation of the regressed ISO, **d** relative vorticity ($s^{-1}$) at 925 hPa, **e** BL moisture convergence ($day^{-1}$) at 925 hPa, **f** convective instability (K), **g** SST (°C) averaged over 80°–100°E from observation (black line) and the model simulations (colored line). The 20–70 day filtered precipitation anomaly averaged over 5°S–5°N and 80°–100°E was used as a reference for calculating regression

to the change of vorticity anomalies (Fig. 6d), indicate that the vorticity anomalies may play a major role in generating BLMC in the EIO. In summary, the model with the modified parameterizations simulates the BLMC to the north of the ISO convention center, which is consistent with its success to simulate the ISO northward propagation.

The enhanced BLMC anomalies may generate a deepen moist lower troposphere in advance of the deep convective phase of the MJO (e.g., Bladé and Hartmann 1993; Johnson et al. 1999; Kemball-Cook and Weare 2001; Tian et al. 2006). In the tropical lower troposphere, the equivalent potential temperature (EPT) change reflects moisture variation because the temperature anomaly is small. To show the moistening and destabilization processes efficiently, we examine the EPT anomalies which also show the moist static energy anomalies of the MJO. Figure 7 shows vertical profiles of the EPT anomalies regressed on the 20–70 day filtered precipitation averaged over the eastern Indian ocean (5°S–5°N, 80°–100°E). The observed shows a peak of the EPT near 500 hPa around the equator since the ISO major precipitation center occurs there. The EPT anomalies extend to the north (~20°N) in the lower troposphere and boundary layer, suggesting that the lower troposphere is moistened ahead of the MJO center. The CTL did not capture the northward extension of the EPT. It shows a southward extension in the lower troposphere, which is consistent with the southward propagation of the ISO convection (Fig. 5b). The CPRCON simulates the northward extension of the EPT in the lower troposphere. However, it simulates positive EPT in the middle and upper troposphere over 20°–30°N, which are not observed. In the SHLC, the southward extension of the ISO is reduced and the northward extension is simulated but it occurs mainly in the boundary layer. The ENTR shows a dominant northward extension of the EPT but the positive EPT extends up to 15°N. In the TRIG, the EPT extends at the north of the BSISO center in the lower troposphere but the magnitude of the EPT is stronger than the observations and other models. The M-TDK reproduces the observed vertical structure of the EPT anomalies with a higher pattern correlation of 0.88 and a lower normalized root-mean-square error of 0.58 when compared to the observation. These results suggest that the modified parameterizations may contribute to the northward propagation of the ISO convection by enhancing the moist boundary layer or lower troposphere.

The increased EPT may induce positive convective instability anomalies to the north of the ISO center (Hsu and Li 2012). Figure 6f shows the meridional structure of the convective instability index (EPT at 850 hPa–EPT at 300 hPa, Yang and Wang 2019) anomalies, which represents

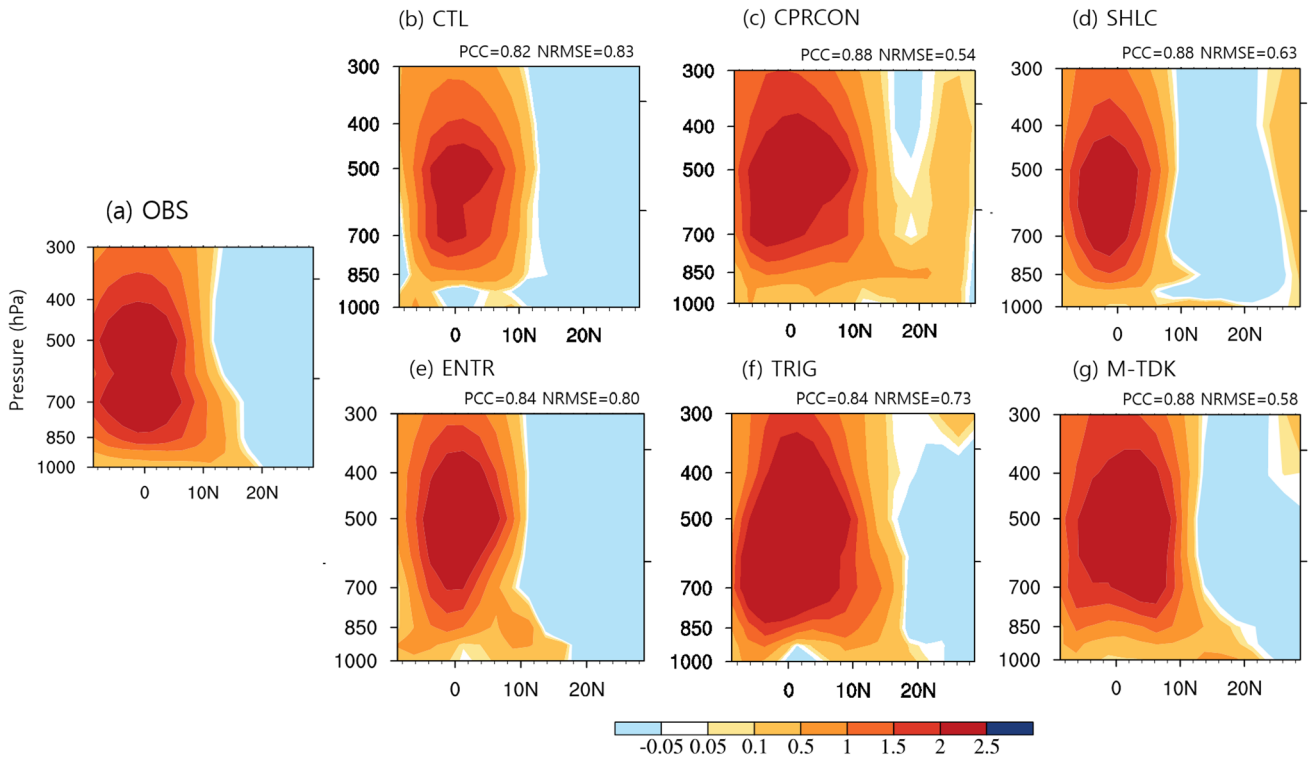


**Fig. 7** Equatorial meridional asymmetry in the equivalent potential temperature (EPT, K) averaged between 80°E and 100°E in **a** the observation and **b**–**g** the model simulations. The structures in each panel are depicted by the regressed 20–70 day filtered EPT onto the 20–70 days filtered precipitation averaged over the BSISO precipitation center (5°S–5°N, 80°–100°E)

destabilization before the ISO deep convection. In observation, convective instability is negative near the equator, where ISO deep convection occurs. It becomes positive at the north (5°N–20°N) of the BSISO center, indicating that the next convection may be generated at the north of the existing BSSO deep convection. The CTL simulates negative convective instability between 20°S and 15°N, suggesting that the CTL fails to indicate the next convection at the north of ISO main deep convection. The ENTR and SHLC produce positive convective instability over 5°N–20°N and the magnitude is comparable with the observation. In the TRIG and CPRCON, positive convective instability extends to 30°N. Note that all models with the modified parameterizations simulate strong negative convective instability around the equator, indicating that the models tend to overproduce the strength of deep convection there. The M-TDK reproduces the observed meridional structure of convective instability, indicating that the M-TDK may generate the next convection at the north of the BSISO center. Note that the M-TDK underproduces the convective instability over 5S°–5°N and overproduces it over 10°–30°N, which is consistent with the meridional distribution of the BLMC (see Fig. 6e).

We examined the eddy potential available energy (EAPE) as shown in Fig. 8. The EAPE is useful to show the energy source of the ISO perturbation. The EAPE is positive when the heating is added in the warm air or cooling occurs in the colder region. Figure 8 shows the EAPE anomalies regressed on ISO convection over EIO. The observation represents a peak of EAPE anomalies over the BSISO center in the middle troposphere (400–500 hPa). In the north of the ISO center in the lower troposphere, positive EAPE anomalies were observed. The zonal asymmetry in the EAPE anomalies concerning the ISO precipitation center or northward extension of the lower tropospheric EAPE anomalies is consistent with those of the EPT. These results indicate that northward propagation of the ISO precipitation may be generated by the positive or higher EAPE anomalies at the north of the BSISO center because the positive EAPE can be converted to eddy kinetic energy. As shown in Fig. 8b, the CTL fails to capture the northward extension of the EAPE in the lower troposphere. The CPRCON, ENTR, and TRIG simulate positive EAPE anomalies in the north of ISO center up to 25°N, which is more extended northward compared to observation. The SHLC simulates weak positive EAPE in the boundary layer. The M-TDK reproduces the observed vertical structure of the EAPE anomalies with a stronger magnitude, suggesting that the modified parameterizations may produce positive EAPE anomalies, which may contribute to northward propagation.

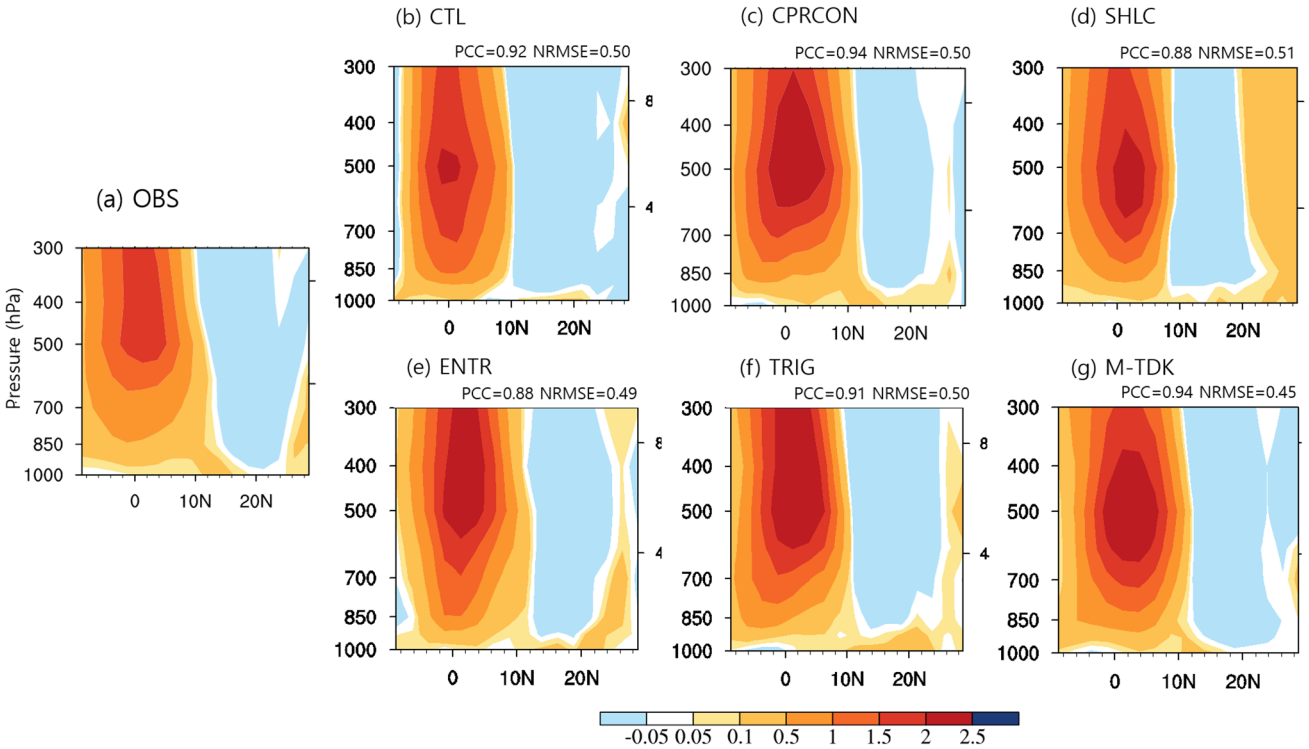


**Fig. 8** Equatorial meridional asymmetry in the BSISO eddy available potential energy (EAPE) generation rate ($K^2$ $day^{-1}$) averaged between 80°E and 100°E in **a** the observation and **b**–**g** the model simulations. The structures in each panel are depicted by the regressed 20–70 day filtered EAPE onto the 20–70 days filtered precipitation averaged over the BSISO precipitation center (5°S–5°N, 80°–100°E)

Other possible mechanisms have been examined to test whether they may be critical for BSISO northward propagation by modified parameterizations or not. We have tested the role of BL moisture advection by the winds (Jiang et al. 2004; DeMott et al. 2013). The meridionally increased mean specific humidity may be favorable with an occurrence of the next convection at the north of the BSISO center. Figure 6b shows the meridional structure of mean specific humidity at 1000 hPa from models and observations. The observation shows low specific humidity anomalies between 20°S and the equator, and it gradually increases at the north of the BSISO precipitation center. It has a peak near 20°N and then decreases around 25°N, suggesting that next convection may occur at the north of the ISO center by abundant moisture anomalies. The CTL produces weaker mean moisture than observation from 20°S to 20°N. The SHLC and CPRCON simulate increased moisture but still less than the observation. The TRIG and ENTR produce more increased moisture at the north of the BSISO center, which is comparable with the observation. The M-TDK shows a realistic meridional structure of moisture over 20°S to 30°N, suggesting that the modified parameterizations can increase the mean moisture profile. Figure 6c shows the meridional structure of the moisture at 850 hPa. The observation shows an increased meridional gradient than that at 1000 hPa (Fig. 6b) over 5°N–25°N. In the CTL, the meridional gradient is much flattened compared to the observation and corresponding moisture gradient at 1000 hPa. The SHLC and CPRCON improve meridional profiles of mean moisture. The TRIG and ENTR enhance not only the mean moisture amount but also the meridional gradient of the moisture, closer to the observed. The M-TDK can capture the observed meridional gradient of the moisture. Comparison between Fig. 6b, c, the modified parameterizations may contribute to enhance upward transport of the moisture from the surface to the lower troposphere at the north of the ISO convection.

We also examined the air-sea interaction mechanism, which may contribute to ISO northward propagation. Figure 6g shows the meridional structure of the SST anomalies regressed on the ISO convection over the EIO. The observation shows strong cold SST anomalies around equatorial EIO, where the ISO precipitation center occurs. The warm SST anomalies at the north of the BSISO center (8°N–25°N) are observed, suggesting that the next convection may be generated at the north of the ISO center. Note that the cold anomalies near the equator are attributed to a reduced downward solar radiation by deep cloud amount. In the CTL, SST anomalies are very weak around the equator, suggesting that the CTL has difficulties capturing ISO deep convection center there. The SST anomalies fluctuate with a very small magnitude from 5°N to 15°N and then become positive, indicating that the CTL partly fails to simulate warmer SST anomalies at the north of the ISO center. The ENTR and SHLC capture warm SST anomalies between 5° and 25°N but fail to simulate cold SST anomalies, implying that the ENTR and SHLC still cannot capture ISO deep convection with a planetary scale shown as in Fig. 4. The CPRCON and TRIG simulate both cold anomalies near the equator and warm anomalies in the north of EIO realistically. The M-TDK also captures the meridional structure of SST anomalies with a stronger magnitude from the equatorial EIO to the Bay of Bengal. These results suggest that the meridional structure of SST anomalies associated with ISO deep convection center may partly contribute to the improved northward movement of ISO convection.

We added the modified parameterizations in the RAS scheme to test whether the modified parameterizations improve the northward propagation of the ISO in another convective scheme (Fig. 9). The RAS fails to capture northward propagation of the ISO; it shows standing ISO features. The M-RAS (The RAS scheme with the modified parameterizations) realistically produces the ISO northward propagation when compared to that of the RAS. The M-RAS well represents the meridional structure of mean vertical shear in the EIO and SST anomalies with respect to the ISO center, which is similar to those of the M-TDK. These results suggested that the modified parameterizations may work in other convective parameterizations. Note that the M-RAS climatology is slightly worse than that of the RAS; The SST is slightly colder than the M-RAS since the M-RAS produces less downward shortwave radiation by more cloudiness.

We examined other climate model simulations, Global Coupled model version 2 (GC2, Williams et al. 2015) and version 3 (GC3, Walters et al. 2011) whether our hypothesis, suppressing convection based on boundary layer properties, could be applied to other climate models. One of the major differences between GC2 and GC3 is that GC3 includes a modified convective trigger based on boundary layer properties and entrainment rate based on convective activities (Williams et al. 2015; Walters et al. 2011). We compared the BSISO simulation of GC2 with that of GC3. Figure 10 shows the latitude-time structure of the lead-lag correlation of BSISO precipitation in the EIO from the GC2 and GC3. We use the ISO convection center at the equatorial EIO (80°–100°E, 5°S–5°N) as a reference because strong BSISO northward propagation occurs there. In observations, the convection of the BSISO moves northward with a phase speed of 1.0 m $s^{-1}$ from equatorial EIO to the Bay of Bengal. The GC2 produces northward propagation of ISO convection but its magnitude is weak. The GC3 shows improved northward propagation of ISO precipitation between 0°N and 25°N with a relatively significant pattern correlation coefficient ($> 0.75$) when compared to the GC2. These results suggest that the GC3 with a convective trigger based

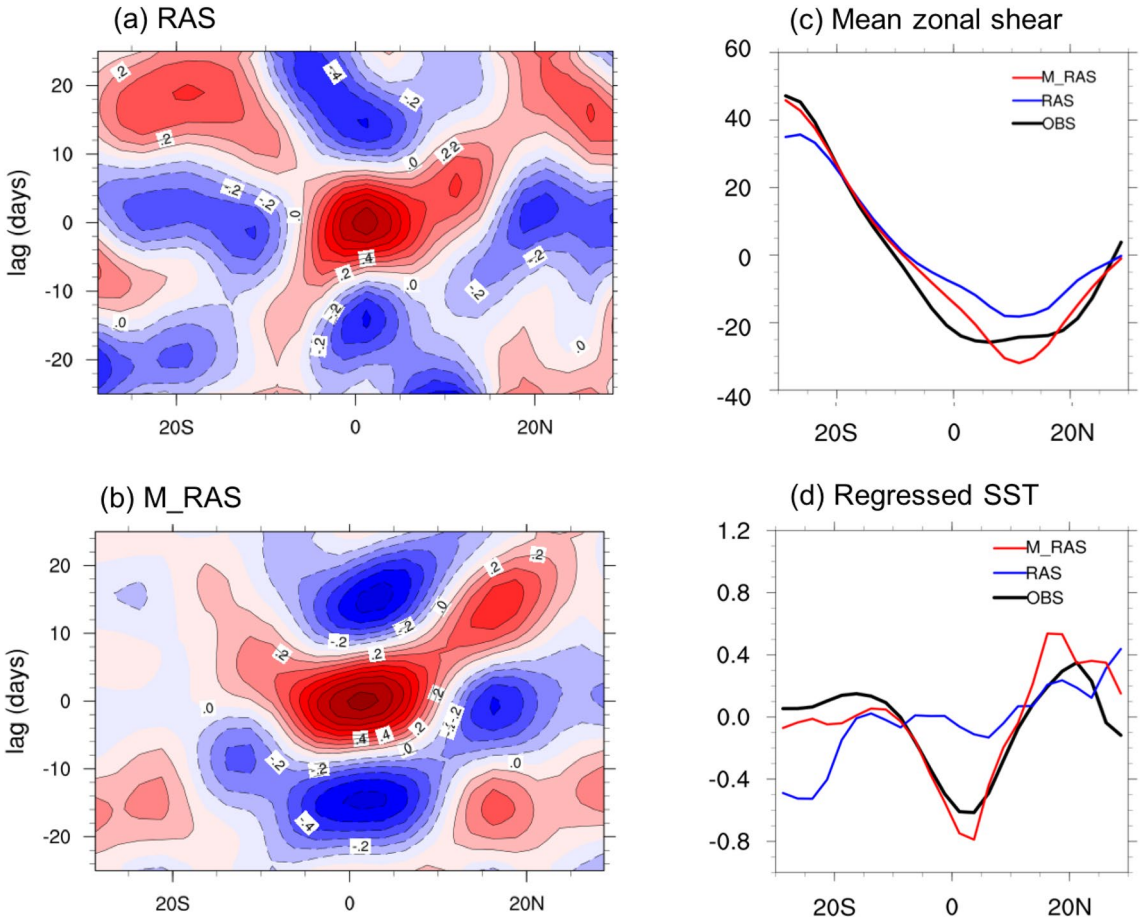


**Fig. 9** **a**, **b** Propagation of ISO precipitation as depicted by the lead-lag correlation of 20–70 day filtered precipitation averaged over 80°–100°E from **a** RAS and **b** M-RAS during boreal summer (May–October). The ISO precipitation averaged over 80°–100°E and 5°S–5°N was used as a reference for calculating the correlation. **c** Meridional structure of June–August mean-state zonal shear (U200–U850, m $s^{-1}$), and **d** Meridional variation of the regressed ISO SST anomalies (°C) averaged over 80°–100°E from observation (black line) and the model simulations (colored line). The 20–70 day filtered precipitation anomaly averaged over 5°S–5°N and 80°–100°E was used as a reference for calculating regression

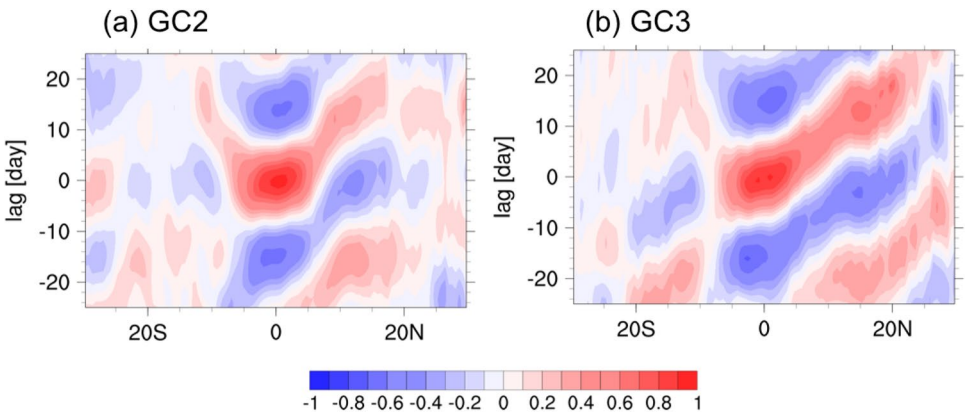


**Fig. 10** Propagation of ISO precipitation as depicted by the lead-lag correlation of 20–70 day filtered precipitation averaged over 80°–100°E from **a** GC2 and **b** GC3 during boreal summer (May–October). The ISO precipitation averaged over 80°–100°E and 5°S–5°N was used as a reference for calculating the correlation

on boundary layer properties tends to improve the northward propagation of the ISO simulation significantly.

Figure 11 shows the composite life cycles of outgoing longwave radiation (OLR) and winds at 850 hPa (U850) from the GC2 and GC3 (phase 2–5) were analyzed to show processes for the evolution and propagation of the BSISO in the models. Eight phases based on the BSISO index are used in the figure using multivariate empirical orthogonal

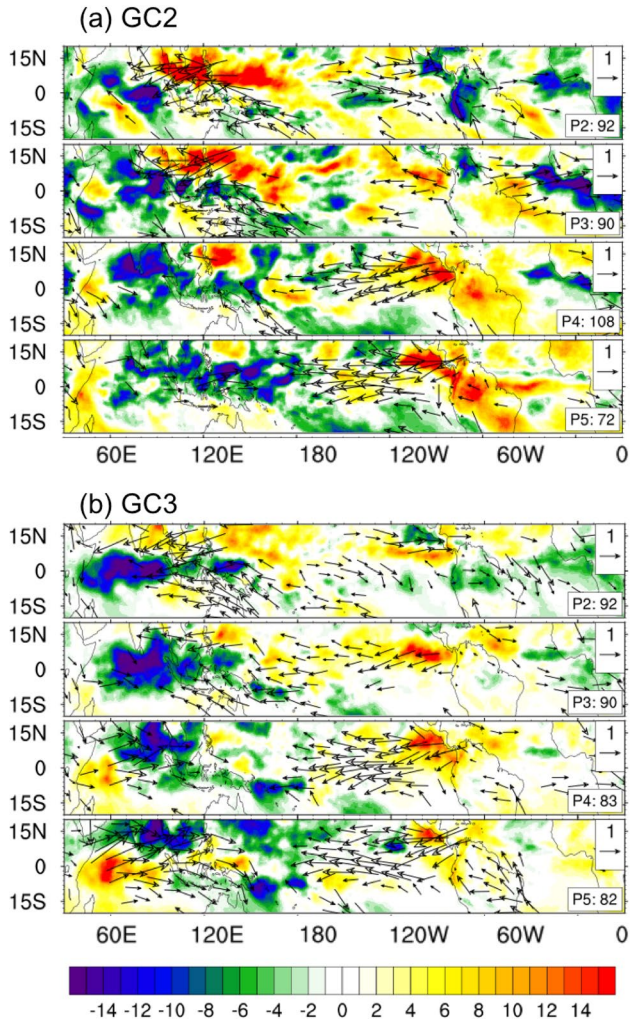


**Fig. 11** The life cycle composite of OLR (shading, W $m^{-2}$) and 850-hPa wind (vector, m $s^{-1}$) anomaly. Wind vectors are shown in the region with statistically significant change at a 95% confidence level based on a t test. We showed the phase 2 to phase 5 (top to bottom) obtained from **a** GC2 and **b** GC3. These phases are calculated by the first two major modes of BSISO during May–October. We first calculated daily anomalies of OLR and zonal wind at 850 hPa (U850) (10°S–10°N, 40°–160°E) and applied multivariate empirical orthogonal function analysis (Lee et al. 2013). Eight phases are defined based on the first and second EOF mode which represents the canonical northward propagating mode

function analysis from daily anomalies of OLR and U850 data during May–October (Lee et al. 2013). The GC2 captures northward propagation of the ISO but the intensity is weaker than observation and the horizontal pattern of the OLR is not organized compared to observation. The weak convective anomalies occur at the eastern Indian ocean in phase 2. The convective anomalies in the eastern Indian ocean become strong and slightly move both southward and northward in phase 3. The convective anomalies move northward in phase 4 and eventually become weak and move to the south of the EIO (phase 5). The GC3 captures the observed northward propagation in the EIO with relatively strong anomalies. The corresponding wind anomalies are also comparable to the observation.

We examine how mean state changes by the modified parameterizations affect the ISO northward propagation over the EIO. The modified parameterization tends to suppress deep convection, while enhances shallow or congest clouds, which changes the MJJASO mean vertical zonal wind shear by modifying temperature and wind fields in the lower and higher troposphere (Fig. 12a). In the observation, dominant easterly vertical shear averaged over the EIO (80°E–100°E) was seen from the EIO and Bay of Bengal (10°S–30°N). The vertical shear has a peak around 10°N and then reduced with increasing latitude. The GC2 simulates weak shear from south of EIO to the Bay of Bengal and its peak is smaller than the observation (10–40%). On the other hand, the GC3 simulates a realistic meridional structure of zonal between 7°N and 20°N compared to the observation.

Figure 12b show vorticity anomalies (925 hPa) regressed on the 20–70 day filtered precipitation averaged over the western Pacific (5°S–5°N, 80°–100°E). Observation shows significant positive vorticity anomalies from 5°N to 15°N, where zonal vertical shear is about 25 m $s^{-1}$. Its peak is located around 10°N, which is consistent with the range of northward propagation of the ISO precipitation center (e.g., Jiang et al. 2004). In the GC2, the positive vorticity anomalies are weak between 5°N and 11°N, which may be consistent with corresponding weak vertical shear. The GC3 simulates strong positive vorticity anomalies from the EIO to 15°N, which are similar to the observed. These results suggest that the changes in vorticity anomalies may be attributed to the magnitude of vertical wind shear. The magnitude of vorticity in the GC3 is almost the same as that of the observation.

We also examined the air-sea interaction mechanism, which may contribute to ISO northward propagation from the GC2 and GC3. Figures 12c show the meridional structure of the SST anomalies regressed on the ISO convection over the EIO. The observation shows strong cold SST anomalies around equatorial EIO, where the ISO precipitation center occurs. The warm SST anomalies at the north of the ISO center (8°N–25°N) are observed, suggesting that the next convection may be generated at the north of the ISO center. Note that the cold anomalies near the equator are attributed to a reduced downward solar radiation by deep cloud amount. In the GC2, SST anomalies are very weak around the equator, suggesting that the GC2 has difficulties capturing ISO deep convection center there. The SST anomalies fluctuate with a small magnitude from 8°N to 20°N, indicating that the GC2 partly fails to simulate warmer SST anomalies at the north of the ISO center. The GC3 also captures the meridional structure of SST anomalies with a stronger magnitude from the equatorial EIO to

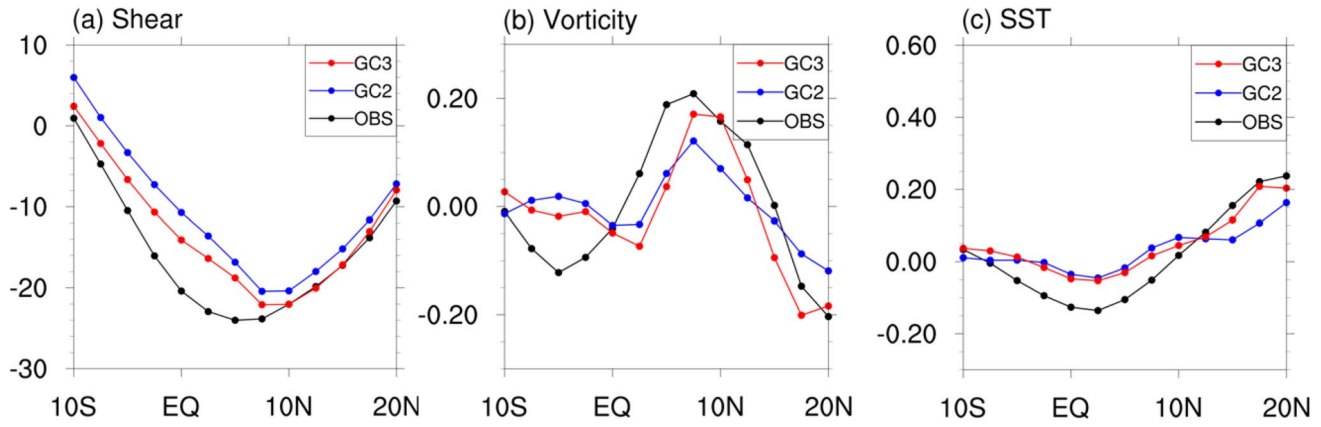


**Fig. 12** Meridional structure of May–October **a** mean-state zonal shear (U200–U850), Meridional variation of the regressed ISO **b** relative vorticity ($s^{-1}$) at 925 hPa, and **c** SST (°C) averaged over 80°–100°E from observation (black line), the GC2 (blue line) and the GC3 (red line) model simulations. The 20–70 day filtered precipitation anomaly averaged over 5°S–5°N and 80°–100°E was used as a reference for calculating regression

the Bay of Bengal. These results suggest that the meridional structure of SST anomalies associated with ISO deep convection center may partly contribute to the improved northward movement of ISO convection.

## 5 Conclusion and discussion

We explore the impact of the modified parameterizations on BSISO northward propagation in the Indian Pacific and how the modified parameterizations affect BSISO simulations using possible mechanisms including vertical zonal wind shear, meridional gradients of the mean specific humidity, and air-sea interaction by examining the NESM3.0 numerical simulations. The modified parameterizations improve the ISO northward systematically from the equatorial eastern Indian Ocean to the Bay of the Bengal.

Analysis of the northward propagating BSISO structure from climate model experiments shows that the modified parameterizations improve BSISO simulations by enhancing vertical zonal wind shear over the EIO. All modified parameterizations produce increased positive vorticity anomalies by enhanced zonal vertical shear compared to the model without the modified parameterizations. The positive vorticity generates increased BLMC, inducing EPT, or moist static energy in the lower troposphere. The enhanced EPT in the lower troposphere increases convective instability to the north of the ISO convection center, generating ISO northward propagation.

Other proposed mechanisms have been tested to explain the improved northward propagation of ISO. Only the modified parameterizations including ENTR and TRIG tends to increase the meridional gradients of the mean moisture over 5°N–25°N, which is consistent with the strengthened northward propagation of ISO convection, whereas the SHLC and CPRCON did not. For the air-sea interaction processes, the modified parameterizations including TRIG and CPRCON improve the meridional structure of SST anomalies over the EIO. The M-TDK shows that all three processes work reasonably well, which is consistent with better BSISO simulation (e.g. Figure 4g). Note that the TRIG also enhances three processes related to the northward propagation of the BSISO, suggesting that the proper suppression of convection may be a key for improving the BSISO simulations. The SHLC improved the BSISO simulations by enhancing "vorticity anomalies by increased zonal shear" and "air-sea interaction", which is consistent with the mechanism or processes suggested by previous studies (Liu et al. 2018; Abhik et al. 2013).

To check whether our hypothesis could be applied to different climate models, we compared the earlier version of the GC model (GC2) with the later version of the GC model (GC3). One of the major differences between GC2 and GC3 is that GC3 includes a modified convective trigger based on boundary layer properties and entrainment rate based on convective activities. The GC3 with a convective trigger based on boundary layer properties tends to improve the northward propagation of the ISO simulation significantly compared to those of the GC2. The modified parameterization in the GC3 improves the meridional structure of zonal shear, positive vorticity, and SST anomalies from the EIO to the Bay of Bengal. These results indicate that our hypothesis may work well in other climate models for the improved northward movement of ISO convection. It is noted that generally speaking, the ISO simulation is sensitive to convective parameterizations (including shallow convective schemes) as well as other physical processes and this topic will be discussed in further study.

**Acknowledgements** This work is funded by the Korea Meteorological Administration Research and Development Program under Grant KMI2020-01310. We acknowledge the Met Office for allowing us to use data from GC2 and GC3 climate model control experiments.

**Author contributions** Y-MY designed the model's overall structure and the strategy for the development of the model. Y-MY and J-AC were responsible for code development and model improvement. Y-MY, K-Y K, J-YM, and BW were responsible for the diagnosis of the model results. Y-MY and J-YM drafted the original paper and BW contributed to revising the paper.

**Code availability** Please contact Young-Min Yang (ymyang@hawaii.edu) to obtain the source code and data for all model experiments.

## Declarations

**Conflict of interest** The authors declare that they have no conflict of interest.

## References

Abhik S, Halder M, Mukhopadhyay P, Jiang X, Goswami B (2013) A possible new mechanism for northward propagation of boreal summer intraseasonal oscillations based on TRMM and MERRA reanalysis. Clim Dyn 40:1611–1624

Adler RF et al (2003) The version-2 global precipitation climatology project (GPCP) monthly precipitation analysis (1979–present). J Hydrometeorol 4(6):1147–1167

Bladé I, Hartmann DL (1993) Tropical intraseasonal oscillations in a simple nonlinear model. J Atmos Sci 50(17):2922–2939

Cao J, Wang B, Yang Y-M, Ma L, Li J, Sun B, Bao Y, He J, Zhou X, Wu L (2018) The NUIST Earth System Model (NESM) version 3: description and preliminary evaluation. Geoscience Model Development 11:2975–2993. https://doi.org/10.5194/gmd-11-2975-2018

Chattopadhyay R, Goswami BN, Sahai AK, Fraedrich K (2009) Role of stratiform rainfall in modifying the northward propagation of monsoon intraseasonal oscillation. J Geophys Res 114:D19114

Dee DP et al (2011) The ERA-Interim reanalysis: Configuration and performance of the data assimilation system. Q J R Meteorol Soc 137(656):553–597. https://doi.org/10.1002/qj.828

DeMott CA, Stan C, Randall DA (2013) Northward propagation mechanisms of the boreal summer intraseasonal oscillation in the ERA-Interim and SP-CCSM. J Clim 26:1973–1992

Drbohlav H-KL, Wang B (2005) Mechanism of the northward propagating intraseasonal oscillation: insights from a zonally symmetric model. J Clim 18:952–972

Fu X, Wang B (2004) Differences of boreal summer intraseasonal oscillations simulated in an atmosphere–ocean coupled model and an atmosphere-only model. J Clim 17:1263–1271

Fu X, Wang B, Li T, McCreary JP (2003) Coupling between northward-propagating, intraseasonal oscillations and sea surface temperature in the Indian Ocean. J Atmos Sci 60:1733–1753

Ganai M, Mukhopadhyay P, Krishna RPM, Abhik S, Halder M (2019) Revised cloud and convective parameterization in CFSv2 improve the underlying processes for northward propagation of Intraseasonal oscillations as proposed by the observation-based study. Clim Dyn 53:2793–2805. https://doi.org/10.1007/S00382-019-04657-9

Goswami BN, Ajayamohan RS, Xavier PK, Sengupta D (2003) Clustering of synoptic activity by Indian summer monsoon intraseasonal oscillations. Geophys Res Lett 30:1431–1434

Halder M, Mukhopadhyay P, Halder S (2012) Study of the microphysical properties associated with the monsoon intraseasonal ocsillation as seen from the TRMM observations. Ann Geophys 30:897–910

Hsu P-c, Li T (2012) Role of the boundary layer moisture asymmetry in causing the eastward propagation of the Madden–Julian Oscillation. J Clim 25(14):4914–4931

Hsu H-H, Weng C-H (2001) Northwestward propagation of the intraseasonal oscillation in the Western North Pacific during the boreal summer: structure and mechanism. J Clim 14:3834–3850

Hsu P-C, Lee J-Y, Ha K-J (2016) Influence of boreal summer intraseasonal oscillation on rainfall extremes in southern China. Int J Climatol 36:1403–1412

Hsu P-C, Lee J-Y, Ha K-J, Tsou C-H (2017) Boreal summer intraseasonal oscillation on heat waves in monsoon Asia. J Clim 30:7191–7211

Jiang X, Li T, Wang B (2004) Structures and mechanisms of the northward propagating boreal summer intraseasonal oscillation. J Clim 17:1022–1039

Johnson RH et al (1999) Trimodal characteristics of tropical convection. J Clim 12(8):2397–2418

Kang I-S, Kim D, Kug J-S (2010) Mechanism for northward propagation of boreal summer intraseasonal oscillation: convective momentum transport. Geophys Res Lett 37:L24804. https://doi.org/10.1029/2010GL045072

Katsumata M, Ciesielski PE, Johnson RH (2011) Evaluation of budget analysis during MISMO. J Appl Meteorol Climatol 50:241–254

Kemball-Cook SR, Weare BC (2001) The onset of convection in the Madden-Julian oscillation. J Clim 14(5):780–793

Kikuchi K, Wang B, Fudeyasu H (2009) Genesis of tropical cyclone Nargis revealed by multiple satellite observations. Geophys Res Lett 36:L06811. https://doi.org/10.1029/2009GL037296

Kim D, Kang IS (2012) A bulk mass fux convection scheme for climate model: description and moisture sensitivity. Clim Dyn 38:411–429. https://doi.org/10.1007/s00382-010-0972-2

Kim D et al (2011) A systematic relationship between intraseasonal variability and mean state bias in AGCM simulations. J Clim 24(21):5506–5520

Kim D et al (2014) Process-oriented MJO simulation diagnostic: moisture sensitivity of simulated convection. J Clim 27(14):5379–5395

Lee MI et al (2001) Influence of cloud–radiation interaction on simulating tropical intraseasonal oscillation with an atmospheric general circulation model. J Geophys Res Atmos 106(D13):14219–14233

Lee JY, Wang B, Wheeler MC, Fu X, Waliser DE, Kang I-S (2013) Real-time multivariate indices for the boreal summer intraseasonal oscillation over the Asian summer monsoon region. Clim Dyn 40:493–509

Lee J-Y, Kwon M, Yun K-S, Min S-K et al (2017) The long-term variability of Changma in the East Asian summer monsoon system: a review and revisit. Asia-Pac J Atmos Sci 53:257–272

Li K, Li Z, Yang Y, Xiang B, Liu Y, Yu W (2015) Strong modulations on the Bay of Bengal monsoon onset vortex by the first northward-propagating intra-seasonal oscillation. Clim Dyn 47:107–115

Liu F, Wang B, Kang I-S (2015) Role of barotropic convective momentum transport in the intraseasonal oscillation. J Clim 28:4908–4920. https://doi.org/10.1175/JCLI-D-14-00575.1

Liu F, Zhao J, Fu X, Huang G (2018) The role of shallow convection in promoting the northward propagation of boreal summer intraseasonal oscillation. Theor Appl Climatol 131:1387–1395. https://doi.org/10.1007/s00704-017-2064-2

Maloney ED, Hartmann DL (2001) The Madden-Julian oscillation, Barotropic dynamics, and North Pacific tropical cyclone formation. Part I: observations. J Atmos Sci 58:2545–2558

Möbis B, Stevens B (2012) Factors controlling the position of the intertropical convergence zone on an aquaplanet. J Adv Model Earth Syst 4(4):M00A04

Moon J-Y, Wang B, Ha K-J, Lee J-Y (2013) Teleconnections associated with Northern Hemisphere summer monsoon intraseasonal oscillation. Clim Dyn 40:2761–2774. https://doi.org/10.1007/s00382-012-1394-0

Moon JY, Wang B, Lee S-S, Ha K-J (2018) An intraseasonal genesis potential index for tropical cyclones during northern hemisphere summer. J Clim 31(22):9055–9071

Neena JM, Waliser D, Jiang X (2017) Model performance metrics and process diagnostics for boreal summer intraseasonal variability. Clim Dyn 48:1661–1683. https://doi.org/10.1007/s00382-016-3166-8

Nordeng TE (1994) Extended versions of the convective parameterization scheme at ECMWF and their impact on the mean and transient activity of the model in the tropics. ECMWF Res Dep Tech Memo. 106

Peters K et al (2017) Improved MJO-simulation in ECHAM6.3 by coupling a stochastic multicloud model to the convection scheme. J Adv Model Earth Syst 9(1):193–219

Simmons A, Uppala S, Dee D, Kobayashi S (2007) ERA-Interim: new-ECMWF reanalysis products from 1989 onwards. ECMWF News 110:25–35

Stephens GL, Vane DG, Boain RJ, Mace GG, Sassen K, Wang Z et al (2002) The cloudsat mission and the a-train. Bull Am Meteorol Soc 83(12):1771–1790. https://doi.org/10.1175/bams-83-12-1771

Tian B et al (2006) Vertical moist thermodynamic structure and spatial–temporal evolution of the MJO in AIRS observations. J Atmos Sci 63(10):2462–2485

Tiedtke M (1989) A comprehensive mass flux scheme for cumulus parameterization in large-scale models. Mon Weather Rev 117(8):1779–1800

Tiedtke M et al (1988) Tropical forecasting at ECMWF: the influence of physical parametrization on the mean structure of forecasts and analyses. Q J R Meteorol Soc 114(481):639–664

Tokioka T et al (1988) The equatorial 30–60 days oscillation and the Arakawa-Schubert penetrative cumulus parameterization. J Meteorol Soc Jpn Ser II 66(6):883–901

Walters DN, Best MJ, Bushell AC, Copsey D, Edwards JM, Falloon PD, Harris CM, Lock AP, Manners JC, Morcrette CJ, Roberts MJ, Stratton RA, Webster S, Wilkinson JM, Willett MR, Boutle IA, Earnshaw PD, Hill PG, MacLachlan C, Martin GM, Moufouma-Okia W, Palmer MD, Petch JC, Rooney GG, Scaife AA, Williams KD (2011) The Met Office Unified Model Global Atmosphere 3.0/3.1 and JULES Global Land 3.0/3.1 configurations. Geosci Model Dev 4:919–941. https://doi.org/10.5194/gmd-4-919-2011

Wang B, Rui H (1990) Dynamics of the coupled moist Kelvin-Rossby wave on an equatorial β-plane. J Atmos Sci 47(4):397–413

Wang B, Xie X (1997) A model for the boreal summer intraseasonal oscillation. J Atmos Sci 54:72–86

Williams KD, Harris CM, Bodas-Salcedo A, Camp J, Comer RE, Copsey D, Fereday D, Graham T, Hill R, Hinton T, Hyder P, Ineson S, Masato G, Milton SF, Roberts MJ, Rowell DP, Sanchez C, Shelly A, Sinha B, Walters DN, West A, Woollings T, Xavier PK (2015) The Met Office Global Coupled model 2.0 (GC2) configuration. Geosci Model Dev 8:1509–1524

Xie X, Wang B (1996) Low-frequency equatorial waves in vertically sheared zonal flow. Part II: Unstable waves. J Atmos Sci 53:3589–3605

Yanai M et al (1973) Determination of bulk properties of tropical cloud clusters from large-scale heat and moisture budgets. J Atmos Sci 30(4):611–627

Yang Y-M, Wang B (2019) Improving MJO simulation by enhancing the interaction between boundary layer convergence and lower tropospheric heating. Clim Dyn 52:4671–4693

Yang J, Wang B, Bao Q (2010) Biweekly and 21–30-day variations of the subtropical summer monsoon rainfall over the Lower reach of the Yangtze River Basin. J Clim 23:1146–1159

Yang YM, Wang B, Li J (2018) Improving seasonal prediction of east Asian summer rainfall using NESM30: preliminary results. Atmosphere 9:487. https://doi.org/10.3390/atmos9120487

Yang Y-M, Lee J-Y, Wang B (2019b) The Tibetan Plateau uplift is crucial for eastward propagation of Madden–Julian Oscillation. Sci Rep 9:15478

Yang Y-M, Wang B, Lee J-Y (2019a) Mechanisms of northward propagation of boreal summer intraseasonal oscillation revealed by climate model experiments. Geophys Res Lett 46:3417–3425

Yang Y-M, Wang B, Cao J et al (2020b) Improved historical simulation by enhancing moist physical parameterizations in the climate system model NESM3.0. Clim Dyn 54:3819–3840

Yang Y-M, Lee J-Y, Wang B (2020c) Dominant process for northward propagation of boreal summer intraseasonal oscillation over the Western North Pacific. Geophys Res Lett 47:e2020GL089808

Yang Y-M, An S-I, Wang B, Park JH (2020a) A global-scale multidecadal variability driven by Atlantic multidecadal oscillation. Natl Sci Rev. https://doi.org/10.1093/nsr/nwz216

Zheng Y, Waliser DE, Stern W, Jones C (2004) The role of coupled sea surface temperatures in the simulation of the tropical intraseasonal oscillation. J Clim 17:4109–4134

Zhu B, Wang B (1993) The 30–60-day convection seesaw between the tropical Indian and western Pacific Oceans. J Atmos Sci 50:184–199